Flexible Electromagnetic Modeling of SMM Setups with FE and FDTD Methods

Arif Can Gungor, *Institute of Electromagnetic Fields(IEF), ETH Zurich*, arifg@ethz.ch
Malgorzata Celuch, *QWED Sp.z o.o*, Warsaw, Poland, mceluch@qwed.eu
Jasmin Smajic, *Institute of Electromagnetic Fields(IEF), ETH Zurich*, jasmin.smajic@ief.ee.ethz.ch
Marzena Olszewska – Placha, *QWED Sp. z o.o.*, Warsaw, Poland, molszewska@qwed.eu
Juerg Leuthold, *Institute of Electromagnetic Fields(IEF), ETH Zurich*, leuthold@ethz.ch

***Abstract*—This paper presents FDTD and FEM modeling of two different types of structures representative of industrial scanning microwave microscopy (SMM) material measurements. The first structure is based on a dielectric resonator where the frequencies of whispering gallery modes have to be known with relative errors below 10^{-4}. Herein, this accuracy has been demonstrated using a FEM code adapted to dielectric anisotropy with hybrid usage of vectoral and nodal elements and FDTD code run in a three-step procedure. The second SMM structure consists of a conductive fine tip with radius 25 nm at a certain height from the sample. The numerical modeling is based on time domain FE (TD-FEM) and FDTD and it extracts the scattering parameters from conductive or dielectric samples. The results are in qualitative agreement and further work on calibration to the port impedance of the experimental setup is currently continued.**

Keywords—Materials modeling, scanning microwave microscopy, dielectric resonators, electromagnetic modeling, frequency and time domain methods, FEM, FDTD

I. Introduction

Developments of new organic and inorganic materials are currently at the focus of industrial needs. The quality and performance of the final manufactured products depend strongly on their chemical/electrical/optical/mechanical properties at nanoscale as well as their arrangements at macroscale. While nanoscale measurements have become feasible [1]-[5], macroscale characterization as in [6]-[9] is needed to verify that the material properties are set correctly on the entire surface of e.g. a thin-film solar cell. To bridge the gap between nano- and macro-scale measurements, and to interpret those measurements into industrially useful knowledge, numerical modeling techniques are needed that replicate the measurement process on a computer and visualize the otherwise invisible physical phenomena.

This work forms a part of our research activities conducted in the framework of the European project MMAMA [10] concerned with scanning microwave microscopy (SMM) and its modeling. SMM is a family of material measurement techniques at microwave frequencies, from micro- to nanoscale. A representative setup for nanoscale are SMM tips [1]-[5], while popular macroscale setups include dielectric resonators [6]-[8]. The modelling of those setups has previously been reported. However, for the tip-to-sample interaction the focus has typically been on a specific problem, for which an overall understanding was required [5]. For dielectric resonators, tailor-made algorithms such as Rayleigh-Ritz coupled to radial mode-matching have been implemented [8] and it is often argued that general-purpose codes are incapable of proving a sufficient accuracy, as stringent as 10^{-4}.

In this paper, we summarize our efforts to apply the popular FEM [11][12] and FDTD [13][14] methods to the analysis of SMM scenarios, with a view to setting up a computer platform flexible in terms of geometry and simulation parameters. Our first goal is to cross-validate the two methods and in Section II, we present the actions performed to achieve their excellent match for an eigenvalue problem concerning a dielectric resonator. In Section III, we extend the FEM and FDTD analysis to a deterministic problem based on an industrial definition of a tip-to-sample interaction, which has so far led to qualitative agreement. In Section IV, further steps planned to be completed by the time of the NEMO Conference are indicated.

II. Eigenvalue Analysis of Dielectric Resonator

For this analysis, a resonator composed of a flat sapphire ring with a supporting rod is chosen as in [8]. There are several advantages of selecting this benchmark, the first one is that its whispering gallery modes have frequencies starting from around 10 GHz which is a useful operating point for SMM. And there are already semi-analytical and experimental results available for some chosen modes [8], which will enable us to have a comparative study. Lastly, the problem can be reduced to 2D using axisymmetry, and this significantly reduces computational effort required.

The benchmark defined in Fig. 1 is solved with parameters $D_c = 80\text{mm}$, $L_c = 50\text{mm}$, $D = 49.9894\text{mm}$, $L = 30.008\text{mm}$, $d = 15\text{mm}$ as in [8]. Sapphire has relative permittivity $\varepsilon_\perp = 9.2747$ in $\text{r} - \phi$ planes while its relative permittivity is $\varepsilon_\parallel = 11.3532$ in z direction in the cylindrical coordinates.

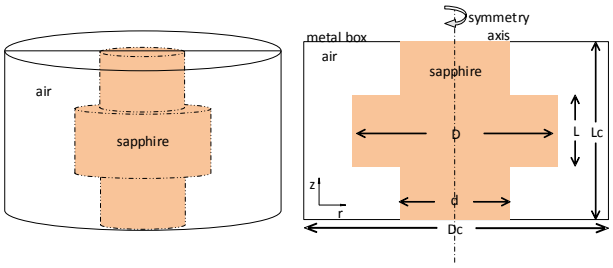

Fig. 1. Visualization of the considered sapphire resonator in 3D (left) and in 2D using axial symmetry (right)

Our first application of the FDTD method to this benchmark has been reported in [15]. The Bodies-of-Revolution formulation after [14] has been adapted into a three-step procedure comprising: resonant frequency extraction of a coarse model with Prony method postprocessing, refined resonance extraction on a refined mesh with Fourier transform, and sine excitation for eigenmode pattern generation. Presently, signal co-processing has been enhanced to accelerate the process to ca. 5 min per frequency, while the results matching those of [8] are maintained and given in Table I (last 3 columns). The modes are named after [8] to account for symmetry and angular dependence of the mode shape.

TABLE I. RESONANT FREQUENCIES OF SELECTED EIGENMODES CALCULATED WITH FEM AND FDTD, VERSUS COMPUTATION AND EXPERIMENT IN [8].

Mode - m	f_{C1} [GHz] comp.[8]	f_{E1} [GHz] exp. [8]	F_{FE} [GHz] FEM	Δf [MHz] $\lvert f_{FE} - f_{C1}\rvert$	Δf [MHz] $\lvert f_{FE} - f_{E1}\rvert$	f_{FD} [GHz] FDTD	Δf [MHz] $\lvert f_{FD} - f_{C1}\rvert$	Δf [MHz] $\lvert f_{FD} - f_{E1}\rvert$
N4- 8	8.51317	8.51281	8.51298	0.19	0.17	8.51286	0.31	0.05
N4- 9	9.19134	9.19115	9.19116	0.18	0.01	9.19122	0.12	0.07
N4-10	9.86408	9.86402	9.86385	0.23	0.17	9.86410	0.02	0.08
N4-11	10.52960	10.53188	10.53155	1.95	0.33	10.53190	2.30	0.02
N4-13	11.85206	11.85500	11.85393	1.87	1.07	11.85438	2.32	0.62
S1-10	8.21869	8.21760	8.21936	0.67	1.76	8.21751	1.18	0.09
S1-11	8.80633	8.80550	8.80674	0.41	1.24	8.80526	1.07	0.26
S1-12	8.39613	9.39560	9.396330	0.20	0.73	9.39500	1.13	0.60
S1-13	9.98764	9.98720	9.98761	0.03	0.41	9.98642	1.22	0.78
S1-14	10.58031	10.58000	10.580154	0.156	0.154	10.57933	0.98	0.67
S1-15	11.17389	11.17380	11.173635	0.255	0.165	11.17305	0.84	0.64

Now an analogous axisymmetric formulation of FEM is derived, starting with the wave equation:

$$\boldsymbol{\nabla} \times \frac{1}{\mu} \boldsymbol{\nabla} \times \boldsymbol{E} - k_0^2 \boldsymbol{\varepsilon_r} \boldsymbol{E} = 0 \tag{1}$$

For the m^{th} azimuthal order, $e^{-jm\phi}$ dependence for each field component in azimuthal direction in cylindrical coordinate system is assumed. The formulation follows the approach of [16] and the anisotropic characteristics of the sapphire are taken into account by decomposing electric field into its in-plane ($\boldsymbol{E_\tau} = E_\tau \boldsymbol{a_\tau} = E_r \boldsymbol{a_r} + E_z \boldsymbol{a_z}$) and azimuthal ($E_\phi \boldsymbol{a_\phi}$) components:

$$\boldsymbol{E} = E_\tau \boldsymbol{a_\tau} + E_\phi \boldsymbol{a_\phi} = \left[\boldsymbol{a_\tau} \sin(m\phi)\, e_\tau + \boldsymbol{a_\phi} \frac{\cos m\phi}{r} e_\phi \right] \tag{2}$$

Using Galerkin's formulation [12] the weak form of (1) can be obtained as in (3), where $\boldsymbol{\nabla_\tau} = \boldsymbol{a_r} \frac{\partial}{\partial r} + \boldsymbol{a_z} \frac{\partial}{\partial z}$, and the superscript "c" denotes the trial function for the corresponding unknown:

$$\iint \left\{ \frac{1}{\mu_r} \left[r(\boldsymbol{\nabla_\tau} \times \boldsymbol{e_\tau^c}) \cdot (\boldsymbol{\nabla_\tau} \times \boldsymbol{e_\tau}) + \frac{m^2}{r} (\boldsymbol{e_\tau^c} \cdot \boldsymbol{e_\tau}) - \frac{m}{r} \left(\boldsymbol{e_\tau^c} \cdot \boldsymbol{\nabla_\tau} e_\phi + \boldsymbol{\nabla_\tau} e_\phi^c \cdot \boldsymbol{e_\tau} \right) + \frac{1}{r} \boldsymbol{\nabla_\tau} e_\phi^c \cdot \boldsymbol{\nabla_\tau} e_\phi \right] - k_0^2 \boldsymbol{\varepsilon_r} \left(r \boldsymbol{e_\tau^c} \cdot \boldsymbol{e_\tau} + \frac{e_\phi e_\phi^c}{r} \right) \right\} dr dz = 0. \tag{3}$$

In order to discretize by using finite elements, vectoral edge elements with linear shape functions are used for in-plane component $\boldsymbol{e_\tau}$ to eliminate possible spurious solutions, and scalar nodal elements with linear shape functions for e_ϕ. Then the matrix form of the eigenvalue equation is obtained as in (4), where $\{e\}$ denotes the eigenvectors and k_0^2 stands for the eigenvalues:

$$[A]\{e\} = k_0^2 [B]\{e\}\,. \tag{4}$$

Solving eigenvalue equation (4) leads the resonant frequency and the mode shape is obtained by back substitution of eigenvector into (2). Field profile obtained by FEM formulation of some chosen mode can be seen in Fig. 2. For FEM solver, a mesh with approximately 80000 elements is used to obtain such accurate results, which has around 120000 edges and 40000 nodes resulting degree of freedom around 160000. A C++ code is compiled as solver, and the complete computation time takes less than 2 minutes with i7 processor. This is several times faster than previously with FDTD, as expected for a deterministic high-Q problem.

The computed eigenfrequencies are included in Table I (columns 4-6) and demonstrate excellent agreement with the FDTD results and reference [8].

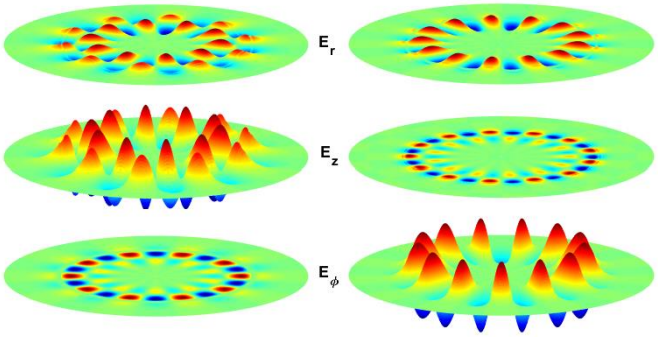

Fig. 2. E-field profile (just above mid-plane) obtained with our axisymmetric FEM for two chosen modes: N4-10 (left) and S1-13 (right).

III. Transient Analysis of SMM Tip

The tip-to-sample SMM problem considered for this analysis is based on an industrial definition [10] and visualized in Fig. 3. It has a straight conductive section above the sample of radius $r_1 = 0.5$ mm, which is tapered into a sharp tip with radius of $r_2 = 25$ nm. The sample is kept at a certain distance of $g = 100$ nm from the tip to account for near field microscopy. Two samples with different properties are considered: metal (gold with $\varepsilon_r = 1$, $\sigma = 4 \cdot 10^7$ S/m) and lossless dielectric (SiN_x of $\varepsilon_r = 8$). Response around 10 GHz band is of interest.

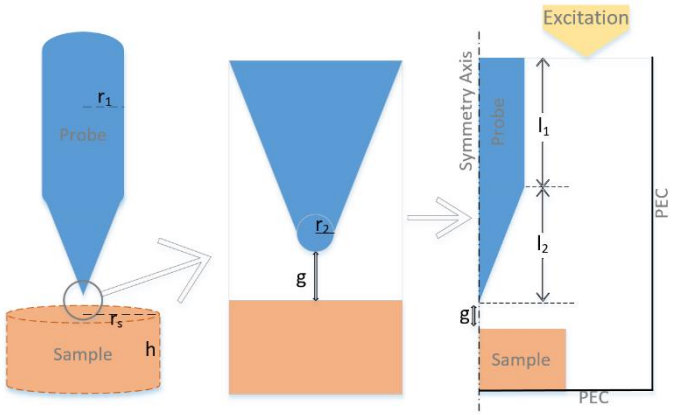

Fig. 3. Visualization of the considered conductive SMM tip in 3D (left), fine tip and the gap (middle) and in 2D using axial symmetry (right).

A general-purpose axisymmetric FDTD code [17] is first applied with quasi-TEM pulse excitation over 8-12 GHz band launched from the upper port in Fig. 3. Space discretization near the fine tip and the air gap can be seen in Fig. 4 for both the solvers. The excitation corresponds to a coax line but is not calibrated to any specific impedance, as the conditions of the experiment in [10] have not been defined in detail. It is observed that FDTD analysis with a standard GPU code does not converge and the reflection coefficient results are corrupted with a numerical noise, after thousands of excitation periods. This is attributed to the very fine meshing at the SMM tip, needed to model the tip and the gap. Therefore, a double-precision version of the FDTD code is implemented and executed on CPU.

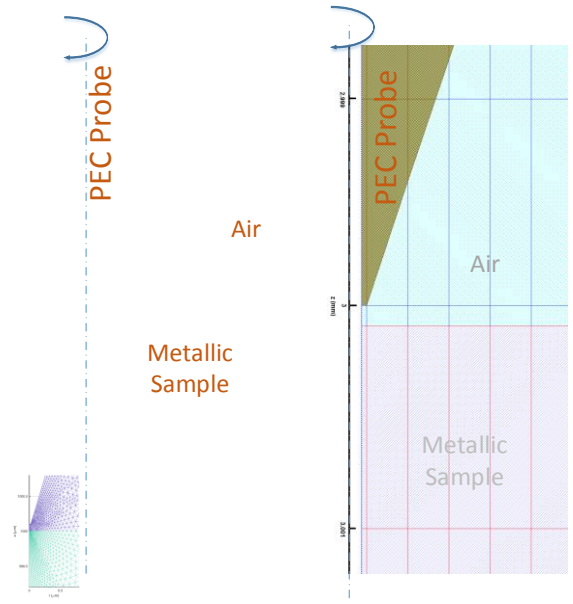

Fig. 4. Very fine discretization near tip for TD-FEM (left) and FDTD (right) solvers.

Now the simulations converge after several excitation periods, after a few seconds simulation on an average laptop computer and z-component of the electric field profile can be seen as in Fig. 5. The required memory is within 1 MB. The effects of both samples are distinguished, as shown in Fig. 6.

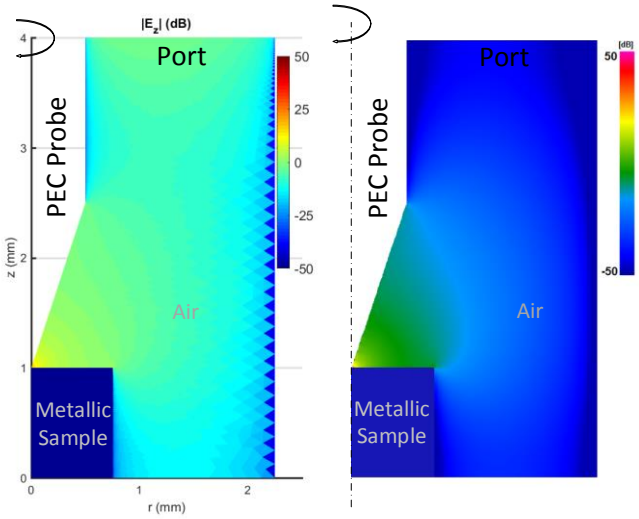

Fig. 5. Amplitude of z-component of E-field profile obtained using TD-FEM (left) and FDTD (right), showing similar behavior with the same port excitation and metallic sample.

To conduct transient FEM simulation, we implement a time-domain algorithm (TD-FEM) with vectoral edge elements and linear shape functions to solve time domain Maxwell's equation for electric field. Then extracting scattering parameters from the port and analyzing Fourier transform of the applied signal would show the effects of different sample properties on reflected power. The following equation governs the transient Maxwell's equation with E-field formulation:

$$\boldsymbol{\nabla} \times \frac{1}{\mu} \boldsymbol{\nabla} \times \boldsymbol{E} + \mu_0 \sigma \frac{\partial \boldsymbol{E}}{\partial t} + \mu_0 \varepsilon_0 \boldsymbol{\varepsilon_r} \frac{\partial^2 \boldsymbol{E}}{\partial t^2} = 0. \tag{5}$$

The boundary condition on the top port is as follows:

$$\boldsymbol{n} \times \left(\frac{1}{\mu} \boldsymbol{\nabla} \times \boldsymbol{E} \right) + \frac{\mu_0}{Z_{Port}} \boldsymbol{n} \times \left(\boldsymbol{n} \times \frac{\partial \boldsymbol{E}}{\partial t} \right) = \frac{-2\mu_0}{Z_{Port}} \boldsymbol{n} \times \left(\boldsymbol{n} \times \frac{\partial \boldsymbol{E_0}}{\partial t} \right), \tag{6}$$

where the bottom and right boundaries of the domain are taken as perfect electric conductor (PEC) ($\boldsymbol{n} \times \boldsymbol{E} = 0$) and the left boundary conditions at $r = 0$ come from the axial symmetry ($\boldsymbol{n} \times \frac{1}{\mu} \boldsymbol{\nabla} \times \boldsymbol{E} = 0$). In the formulation, $\boldsymbol{n}$ denotes the normal vector to the respective boundary, Z_{Port} is the wave impedance at the port and $\boldsymbol{E_0}$ is the input excitation field from the port, which is in time domain a well-known Gaussian burst with center frequency of 10 GHz [11]. The weak form of the equation obtained is

$$\iint \left\{ r\left(\frac{1}{\mu}\nabla \times \boldsymbol{E}\right) \cdot (\nabla \times \boldsymbol{E^c}) + \mu_0 \sigma r \boldsymbol{E^c} \cdot \frac{\partial \boldsymbol{E}}{\partial t} + \mu_0 \varepsilon_0 \varepsilon r \boldsymbol{E^c} \cdot \frac{\partial^2 \boldsymbol{E}}{\partial t^2} \right\} dS + \frac{\mu_0}{Z_{Port}} \int r(\boldsymbol{n} \times \boldsymbol{E^c}) \cdot \left(\boldsymbol{n} \times \frac{\partial \boldsymbol{E}}{\partial t}\right) dl = \frac{-2\mu_0}{Z_{Port}} \int r(\boldsymbol{n} \times \boldsymbol{E^c}) \cdot \left(\boldsymbol{n} \times \frac{\partial \boldsymbol{E_0}}{\partial t}\right) dl, \quad (7)$$

to be computed within the domain, where one-dimensional integrals are only over the port. Also $\boldsymbol{E^c}$ denotes trial function for unknown$\boldsymbol{E}$. For the time discretization backward difference formula (BDF) is used as in (8) where subscripts denote the time step and (7) is solved for $\boldsymbol{E_t}$ after substituting (8).

$$\frac{\partial \boldsymbol{E}}{\partial t} \approx \frac{\boldsymbol{E_t} - \boldsymbol{E_{t-1}}}{\Delta t} \quad (8)$$

For the structure defined in Fig. 3 the implemented FEM solver uses a mesh with around 85000 elements with very fine elements around the sharp tip, 127000 edges (degree of freedom) requiring memory of around 4 GB, including the memory needed to store all field values for later visualization. A corresponding C++ code is compiled. For the simulated example case, around 1000 time steps with $\Delta t = 2$ps are needed for the analysis to converge, which takes less than 10 minutes of computation time. Hence, contrary to the resonator example, now FEM is more computationally expensive than FDTD, both in terms of memory and simulation time.

After solving time domain Maxwell's equation electric field profile is obtained as in Fig. 5 and the port parameters are extracted to obtain the scattering parameters as in Fig. 6. Note however, that the exact conditions of the experiment [10] are not known at the time of collating these results, and hence neither FDTD nor FEM simulations are calibrated to the actual reference impedance. This is why the absolute values of the reflection coefficient calculated with FDTD and FEM are different. They are still consistent (with each other and with the experiment) in showing that metal sample causes lower reflections than the dielectric sample, and that reflections decrease with frequency, also field profiles obtained from both models are quite similar as in Fig. 5. Further work on calibration of the models is also under way.

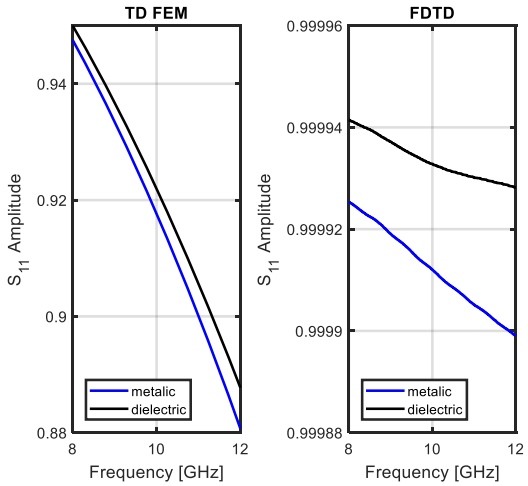

Fig. 6. Reflection from metalic and dielectric samples with tip-to-sample gap of 100 nm obtained with FDTD (right) and TD-FEM (left), without port calibration.

IV. Conclusions

In this work, FDTD and FEM methods have been applied to two scenarios representative of industrial SMM material measurements: a dielectric resonators and a tip-to-sample interface. Since the scenarios are axially symmetrical, computationally effective 2D bodies-of-revolution variants of both methods are applicable. For axisymmetric FDTD, the version available in [17] has been used as a starting point but adapted to the high accuracy requirements of the SMM. Namely, a three-step procedure after [15] has been followed (and here accelerated) for the resonator problem and a double-precision version has been implemented in order to resolve the effects of material samples on the tip. For FEM, two original algorithms have been developed, one utilizing angular mode expansion with material anisotropy in frequency domain and using hybrid elements for high accuracy. And the other being a transient time-domain solver where edge elements are used with local refinement at the sharp tip.

For the eigenvalue problem, FEM and FDTD are in excellent agreement: and both produce frequencies of whispering gallery modes with accuracy of relative error within 10^{-4}, which was previously considered feasible only with tailor-made quasi-analytical methods. For the transient problem, FEM and FDTD are able to simulate the structure and detect the minimal effects of the material samples on the reflection coefficient of the scenario. They are consistent with the measurements [10] in indicating the higher reflections caused by the dielectric as compared to the metal, and the decrease of reflections with frequency. However, further work is required on calibrating both simulations to the reference impedance of the experimental setup. As expected, FEM approach proves faster than FDTD for the high-Q resonator problem, while FDTD is more effective than TD-FEM for the transient problem.

The advantage of adapting FEM and FDTD to SMM modeling is that they offer full flexibility to further simulate arbitrary geometries (of SMM tips or resonators), under real-life measurement conditions and to advanced materials. Currently, a drift-diffusion FEM solver is under development, which will be coupled to the EM algorithms as reported herein, for multiphysics simulations of material measurements in semiconductor industry.

ACKNOWLEDGMENT

The work presented in this paper has received funding from the European Union's Horizon 2020 research and innovation programme (H2020-NMBP-07-2017) under grant agreement MMAMA n°761036.

REFERENCES

[1] Lee, J. H., S. Hyun, and K. Char., "Quantitative analysis of scanning microwave microscopy on dielectric thin film by finite element calculation," Review of Scientific Instruments 72.2 (2001).

[2] Steinhauer, D. E., et al., "Quantitative imaging of dielectric permittivity and tunability with a near-field scanning microwave microscope," Review of Scientific Instruments 71.7 (2000).

[3] Lai, K., et al., "Modeling and characterization of a cantilever-based near-field scanning microwave impedance microscope," Review of scientific instruments 79.6 (2008).

[4] Wei, T., et al. "Scanning tip microwave near- field microscope." Applied Physics Letters 68.24 (1996).

[5] J. Hoffmann, G. Gramse, J. Niegemann, M. Zeier, and F. Kienberger, "Measuring low loss dielectric substrates with scanning probe microscopes," Appl. Phys. Lett. 105, 013102 (2014).

[6] J. Krupka, A. P. Gregory, O. C. Rochard, R. N. Clarke, B. Riddle, and J. Baker-Jarvis, "Uncertainty of complex permittivity measurements by split-post dielectric resonator technique", J. Eur. Ceramic Soc., vol. 21, pp. 2673-2676, 2001.

[7] J. Krupka and J. Mazierska, "Contactless measurements of resistivity of semiconductor wafers employing single-post and split-post dielectric-resonator techniques," IEEE Trans. Instr. Meas., vol. 56, no. 5, pp. 1839-1844, Oct. 2007.

[8] J. Krupka et al., "Use of whispering-gallery modes for complex permittivity determinations of ultra-low-loss dielectric materials," IEEE Transactions on Microwave Theory and Techniques 47.6 (1999).

[9] M. Abu-Teir et al, "Near-field scanning microwave probe based on a dielectric resonator," Review of Scientific Instruments 72.4 (2001).

[10] H2020 MMAMA project reports. [Online]. Available: www.mmama.eu

[11] J. Jin, The Finite Element Method in Electromagnetics, 3rd ed. New York, NY, USA: Wiley, 2014.

[12] J. Smajic, How to Perform Electromagnetic Finite Element Analysis, Hamilton, UK: NAFEMS Ltd., 2016.

[13] A. Taflove and S. Hagness, *Computational Electrodynamics - The Finite-Difference Time-Domain Method*, 3rd Edition, Artech House, Boston-London, 2005.

[14] M. Celuch and W. K. Gwarek, "Industrial design of axisymmetrical devices using a customized FDTD solver from RF to optical frequency bands", *IEEE Microwave Mag.*, vol. 6, no. 9, pp. 150-159, Dec. 2008.

[15] M. Celuch and W. Gwarek, "Accurate analysis of whispering gallery modes in dielectric resonators with BoR FDTD Method", 22nd International Microwave and Radar Conference MIKON 2018, 15-17 May 2018, Poznan, Poland.

[16] J. -F. Lee, G. M. Wilkins, and R. Mittra, "Finite-element analysis of axisymmetric cavity resonator using a hybrid edge element technique," IEEE transactions on microwave theory and techniques 41.11 (1993).

[17] QuickWave EM Software (1997-2018). [Online]. Available: www.qwed.eu